

Computational Insight into the Alkane-
Hydroxylation Mechanism by Non-Heme
Fe(PyTACN) Iron Complexes. Effect of the
Substrate and Solvent

Verònica Postils, Anna Company, Miquel Solà, Miquel Costas* and Josep M. Luis**

Institut de Química Computacional i Catàlisi (IQCC) and Departament de Química,
Universitat de Girona, Campus de Montilivi, 17071 Girona, Catalonia, Spain.

ABSTRACT

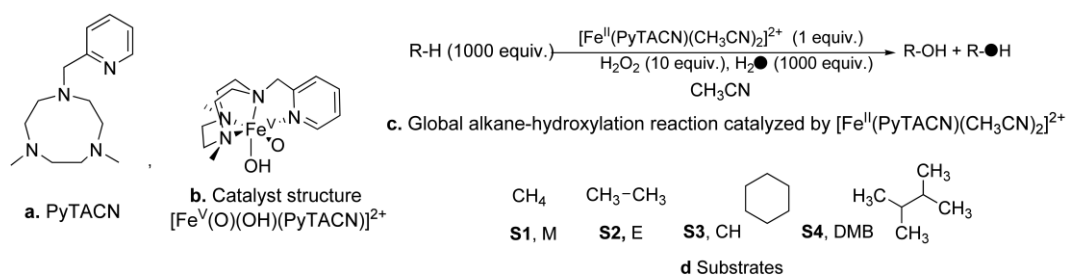
The reaction mechanisms for alkane oxidation processes catalyzed by non heme $\text{Fe}^{\text{V}}\text{O}$ complexes presented in literature vary from rebound stepwise to concerted highly asynchronous processes. The origin of these important differences is still not completely understood. Herein, in order to clarify this apparent inconsistency, the stereospecific hydroxylation of a series of alkanes (methane and substrates bearing primary, secondary, and tertiary C–H bonds) through a $\text{Fe}^{\text{V}}\text{O}$ species, $[\text{Fe}^{\text{V}}(\text{O})(\text{OH})(\text{PyTACN})]^{2+}$ (PyTACN = 1-(2'-pyridylmethyl)-4,7-dimethyl-1,4,7-triazacyclononane), has been computationally examined at gas-phase and in acetonitrile solution. The initial breaking of the C–H bond can occur via hydrogen atom transfer (HAT) leading to an intermediate where there is an interaction between the radical substrate and $[\text{Fe}^{\text{IV}}(\text{OH})_2(\text{PyTACN})]^{2+}$ or through hydride transfer to form a cationic substrate interacting with the $[\text{Fe}^{\text{III}}(\text{OH})_2(\text{PyTACN})]^+$ species. Our calculations show that: i) Except for methane in the rest of the alkanes studied the intermediate formed by R^+ and $[\text{Fe}^{\text{III}}(\text{OH})_2(\text{PyTACN})]^+$ is more stable than that involving the R^\bullet and the $[\text{Fe}^{\text{IV}}(\text{OH})_2(\text{PyTACN})]^{2+}$ complex; ii) In spite of i), the first step of the reaction mechanism for all substrates is a HAT instead of hydride abstraction; iii) The HAT is the rate determining step for all analyzed cases; and iv) The barrier for the HAT decreases along methane \rightarrow primary \rightarrow secondary \rightarrow tertiary carbon. The second part of the reaction mechanism corresponds to the rebound process. Therefore, the stereospecific hydroxylation of alkane C–H bonds by non-heme $\text{Fe}^{\text{V}}(\text{O})$ species occurs through a rebound stepwise mechanism that resembles that taking place at heme analogues. Finally, our study also shows that to properly describe alkane hydroxylation processes mediated by $\text{Fe}^{\text{V}}\text{O}$ species, it is essential to consider the solvent effects during geometry optimizations. The use of gas-phase

geometries explains the variety of mechanisms for the hydroxylation of alkanes reported in the literature.

I. Introduction

Reactions involving functionalization of alkane C–H bonds are of interest because they enable reactivity into otherwise inert molecules.^{1,2} Alkane hydroxylation processes (AHP) have importance in enzymatic oxidations that participate in metabolic paths, xenobiotic detoxification and biodegradation, among others.^{3–6} Furthermore, alkane C–H oxidation reactions find major interest in current organic synthesis.^{7,8} Particularly interesting are C–H oxidation processes mediated by iron based species that occur with retention of the configuration at the hydroxylated carbon. Stereospecific hydroxylations find ample precedent in iron oxygenases, being cytochrome P-450 a paradigmatic case.³ However, they are difficult to reproduce with synthetic complexes because the combination of oxidants with iron compounds very easily results in the formation of Fenton like free diffusing radical processes.^{8–14} The preparation of non-heme Fe^{IV}(O) complexes during the last decade has represented a major step forward reproducing the chemistry taking place at non-heme iron dependent oxygenases, and has prompted the investigation of their reactivity in alkane C–H oxidation.^{15,16}

Scheme 1. Ligand (**a**), catalyst (**b**), and substrates (**d**) used in this study. Global alkane-hydroxylation reaction catalyzed by the studied catalyst (**c**).

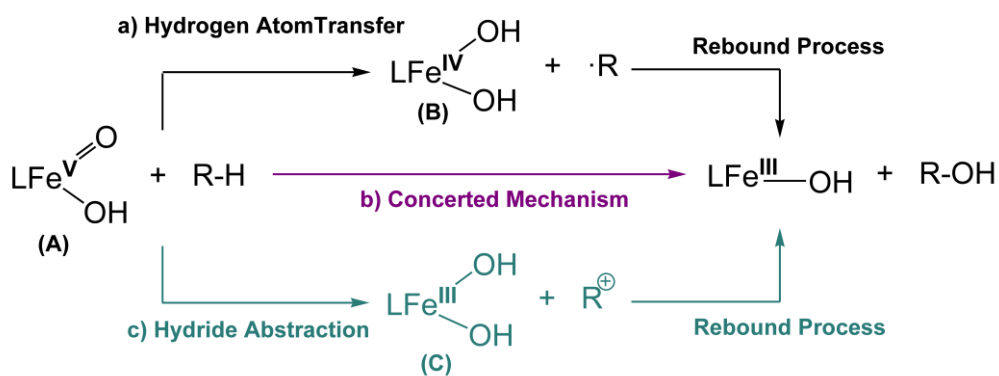


Non-heme $\text{Fe}^{\text{IV}}(\text{O})$ complexes have been shown to be capable of breaking the strong C–H bond of alkanes via a hydrogen atom transfer (HAT) reaction.^{17,18} Close investigation of these reactions shows that long-lived carbon centered radicals are produced after the initial HAT.^{19,20} Thus, these reactions fundamentally depart from stereoretentive processes. In parallel studies, a series of iron complexes containing aminopyridine ligands have been shown capable of mediating stereospecific C–H hydroxylation reactions upon reaction with hydrogen peroxide, and therefore their mechanism of action does not involve generation of free diffusing radicals.^{9–11,21}

Among the non-heme iron complexes that are catalytically active in AHP we can mention the perferryl $[\text{Fe}^{\text{V}}(\text{O})(\text{OH})(\text{PyTACN})]^{2+}$ (PyTACN = 1-(2'-pyridylmethyl)-4,7-dimethyl-1,4,7-triazacyclononane) species, that is formed upon reaction of the $[\text{Fe}^{\text{II}}(\text{CF}_3\text{SO}_3)_2(\text{PyTACN})]^{2+}$ catalysts with excess of H_2O_2 in acetonitrile (Scheme 1a-c). The capability of perferryl complexes to catalyze AHP has been proven experimentally and computationally.^{22–24} This reaction occurs with stereoretention at the hydroxylated carbon site, indicating that long-lived carbon centered radicals or cations are not involved. Other complexes studied in the literature that have also been proposed to involve $\text{Fe}^{\text{V}}(\text{O})$ species include: $[\text{Fe}^{\text{V}}(\text{O})(\text{OH})(\text{L})]^{2+}$ (where L = TPA (TPA=tris(2-pyridylmethyl)amine) and related),^{21,25} $[\text{Fe}^{\text{V}}(\text{O})(\text{L})]^+$ (where L = dpq (dpq=2-[bis(pyridin-2-ylmethyl)]amino-N-quinolin-8-yl-acetamidate),²⁶ and $[\text{Fe}^{\text{V}}(\text{O})(\text{TAML})]^-$ (TAML= tetraamido macrocyclic ligand) and related.^{27–29} However,

the reaction mechanisms for alkane oxidation processes catalyzed by $\text{Fe}^{\text{V}}(\text{O})$ complexes presented in literature show important differences among them, whose origin is not completely understood.^{23,25,29-31} In all cases reaction of the $\text{Fe}^{\text{V}}(\text{O})$ (**A**) species with an alkane starts with a hydrogen-atom transfer (HAT) from the C–H bond by the iron-oxo group and then several different hypothetical pathways are proposed (Scheme 2). The most accepted one is the “rebound mechanism” where the HAT forms an alkyl radical intermediate (R^{\bullet}) that interacts with a bishydroxo $\text{Fe}^{\text{IV}}(\text{OH})_2$ species (**B**) that leads to the final hydroxylated products (Path *a* in Scheme 2). This rebound mechanism for alkane hydroxylation catalyzed by non-heme $\text{Fe}^{\text{V}}(\text{O})$ species was proposed in previous density functional theory (DFT) studies as, for instance, in a work of methane and acetonitrile hydroxylation by $[\text{Fe}^{\text{V}}(\text{O})(\text{OH})(\text{TPA})]^{2+}$.²⁵

Scheme 2. Proposed mechanism for alkane hydroxylation processes by $\text{Fe}^{\text{V}}(\text{O})(\text{OH})(\text{L})$ catalysts.



A second proposed mechanism involves direct formation of the hydroxylated products through a concerted highly asynchronous mechanism (Path *b* in Scheme 2). The transition state in this single step process is given by the HAT, which is followed by the C–O bond formation without the generation of any intermediate. For instance, this asynchronous concerted mechanism was proposed for the cyclohexane

hydroxylation catalyzed by $[\text{Fe}^{\text{V}}(\text{O})(\text{OH})(\text{L})]^{2+}$ (L = tetradentate bispidine ligand)³² and by $[\text{Fe}^{\text{V}}(\text{O})(\text{OH})(\text{PyTACN})]^{2+}$.²³ Finally, in the present work we show (*vide infra*) that a third pathway where a hydride transfer process leads to a cationic alkyl intermediate (R^+) and a bishydroxo $\text{Fe}^{\text{III}}(\text{OH})_2(\text{L})$ unit (C) cannot be *a priori* discarded. Transfer of one of the hydroxide ligands to R^+ would afford the final hydroxylated product (Path *c* in Scheme 2). This third option is similar to the proposed mechanism for the cyclohexane chlorination by $[\text{Fe}^{\text{V}}(\text{O})(\text{Cl})(\text{TPA})]^{2+}$.³⁰ Therefore, depending on the substrate, catalysts, and method of calculation several authors arrived at different conclusions about the operative mechanism in AHP (Scheme 2). A fourth possible mechanism where the substrate radical formed via HAT dissociates and reacts with a second oxo-iron compound to give the corresponding hydroxylated product is also described in literature. This dissociative mechanism has been proposed for the hydroxylation of alkanes catalyzed by $[\text{Fe}^{\text{IV}}(\text{O})(\text{Bn-TPEN})]^{2+}$,³¹ $[\text{Fe}^{\text{IV}}(\text{O})(\text{N4Py})]^{2+}$ ³¹ and $[\text{Fe}^{\text{V}}(\text{O})(\text{TAML})]$,^{28,29} and in these three cases the dissociative mechanism is supported by theoretical and experimental evidences. Furthermore, Gupta and coworkers suggested that the oxidation of the cyclohexane catalyzed by their synthesized biuret-substituted TAML ligand $\text{Fe}^{\text{V}}\text{O}$ compound may proceed by either a rebound mechanism, a dissociative mechanism or a combination of both.²⁸ Then, in principle it is plausible to propose that dissociation of the substrate radical could be competitive with or preferable to the rebound pathway. However, for the particular case of the $[\text{Fe}^{\text{V}}(\text{O})(\text{OH})(\text{PyTACN})]^{2+}$ compound, all the experimental evidences conclusively discard the dissociation mechanism, (see below) and because of that it has not been studied here.

The main goal of this work is to gain insight into the reaction mechanism of AHP studying the hydroxylation of methane, ethane, cyclohexane, and 2,3-dimethylbutane

catalyzed by the $[\text{Fe}^{\text{V}}(\text{O})(\text{OH})(\text{PyTACN})]^{2+}$ complex (Scheme 1). The studied alkanes were chosen because they bear different types of C–H bonds (methane, primary, secondary, tertiary). Our aim is to investigate whether hydroxylation of C–H bonds of different nature proceeds or not through different reaction pathways. A second goal is to analyze how solvent affects the reaction mechanism of AHP. To this end, we performed calculations i) at gas-phase, ii) at gas-phase including single-point energy corrections for dispersion and acetonitrile solvent effects, iii) and in acetonitrile solution (see Computational Details section for more details). The final goal of this study is to identify the key steps of the AHP mechanism to get a better understanding of these reactions that ultimately should help the design of more efficient catalysts.

II. Computational Details

All values presented in this computational study have been obtained with the Gaussian 09 software package³³ using the spin-unrestricted UB3LYP^{34,35} hybrid DFT functional in conjunction with the SDD basis set and the associated effective core potential (ECP) for Fe³⁶ and the 6-311G(d,p) basis set for the rest of the atoms. All geometry optimizations were performed without symmetry constraints. Analytical Hessians were computed to determine the nature of stationary points (one and zero imaginary frequencies for transition states and minima, respectively). Furthermore, the connectivity between stationary points was unambiguously established by intrinsic reaction path calculations.^{37,38}

All final reported energy values were systematically corrected after geometry optimization by removing spin-contamination using the following expressions:^{39,40}

$$E_{spin\ corr} = \frac{E_S - a \cdot E_{(S+1)}}{1 - a} \quad (1)$$

$$a = \frac{\langle S_S^2 \rangle - S \cdot (S+1)}{\langle S_{(S+1)}^2 \rangle - S \cdot (S+1)} \quad (2)$$

where E_S and $\langle S_S^2 \rangle$ are the UB3LYP/6-311G(d,p)~SDD electronic energy and square total spin angular momentum of the S spin state obtained by means of an unrestricted calculation. $E_{(S+1)}$ and $\langle S_{(S+1)}^2 \rangle$ are the electronic energy and square total spin angular momentum obtained for the (S+1) spin state computed with the same level of theory and at the geometry of the S spin state. $E_{spin\ corr}$ is the spin-corrected electronic energy.

From this general level of theory, three different computational methodologies were used. First, we calculated relative gas-phase Gibbs energy values (ΔG_g) including spin-corrected UB3LYP/6-311G(d,p)~SDD electronic energies ($E_{spin\ corr}^g$), together with thermal and entropy corrections at 298.15K obtained from frequency calculations (G_{corr}^g) (Eq. (3)). Second, we obtained relative Gibbs energies (ΔG_{g+corr}) that included relative gas-phase Gibbs energy values plus single-point Gibbs solvation energies in acetonitrile solution ($G_{solv\ corr}^g$) and dispersion corrections (E_{disp}^g) (Eq. (4)). Dispersion effects were calculated using the Grimme DFT-D2 method,⁴¹ whereas solvation effects were computed using the Polarizable Continuum Model - SMD method developed by Truhlar and coworkers, which is based on the quantum mechanical charge density of the solute molecule interacting with a continuum description of the solvent.⁴² The solvent contribution was obtained as the difference between the electronic energy at gas-phase and in solution both computed with the B3LYP method and the 6-31G(d) basis set, the basis set used to parameterize the SMD method. All calculated solvation Gibbs energies use a standard state of an ideal

gas at a gas-phase concentration of $1 \text{ mol}\cdot\text{L}^{-1}$ dissolving as an ideal dilute solution at a liquid-phase concentration of $1 \text{ mol}\cdot\text{L}^{-1}$. The change of conventional 1 atm standard state for gas-phase calculations to a standard-state gas-phase concentration of 1 M requires the introduction of a concentration-change term of 1.89 kcal/mol at 298.15 K, $\Delta G^{o/*}$. Finally, in the third computational methodology used (ΔG_{solv}), the effect of the acetonitrile solution and the D2 dispersion corrections were taken into account during geometry optimization processes at the UB3LYP/6-311G(d,p)~SDD level of theory ($E_{spin\ corr}^{solv} + E_{disp}^{solv} + G_{solv\ corr}^{solv}$), instead of being added through single-point energy calculations at the gas-phase optimized geometries (Eq. (5)). Then, following the approach suggested by Cramer *et al.*, Gibbs energy corrections at 298.15K obtained from frequency calculations at the solvent-phase optimized geometries (G_{corr}^{solv}) were added.⁴³ We can summarize the energy contributions included in each approach as follows:

$$G_g = E_{spin\ corr}^g + G_{corr}^g \quad (3)$$

$$G_{g+corr} = E_{spin\ corr}^g + E_{disp}^g + G_{solv\ corr}^g + G_{corr}^g + \Delta G^{o/*} \quad (4)$$

$$G_{solv} = E_{spin\ corr}^{solv} + E_{disp}^{solv} + G_{solv\ corr}^{solv} + G_{corr}^{solv} + \Delta G^{o/*} \quad (5)$$

Except otherwise noted, energies discussed in this work were obtained using Eq. (5). In the Supporting Information, we provide Tables with energies obtained using Eqs. (3) and (4).

The rigorous accurate computational study of electron transfer (ET) processes in solvent requires expensive multiconfigurational calculations in order to describe electronic states properly. Moreover, the search of the ET barrier in solution, at UB3LYP/SMD level of theory, did not yield a good description of the barrier.

UB3LYP/SMD led to abrupt changes on the potential energy surfaces instead of a smooth description of the ET potential energy profile even when the more flexible IEFPCM model was used.⁴⁴ In this work, to compute the ET barriers, we used the widely accepted classical Marcus formalism.^{45,46} The Marcus theory uses the Gibbs energy of the redox reaction ($\Delta G^o = \Delta G_{prod} - \Delta G_{react}$) and the reorganization energy (λ) to calculate the ET Gibbs energy barrier (ΔG^*) through:

$$\Delta G^* = \frac{(\Delta G^o + \lambda)^2}{4\lambda} \quad (6)$$

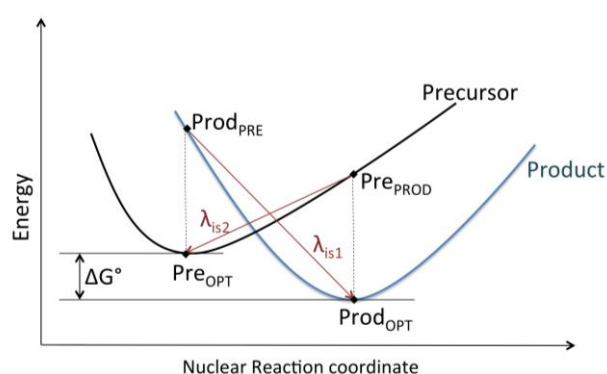


Figure 1. Schematic illustration of the procedure used for the calculation of inner sphere reorganization energies (λ_{is}).

The reorganization energy (λ) is the energy change due to the whole chemical system (the complex and the surrounding solvent molecules) rearrangement. It splits into inner sphere reorganization energies, λ_{is} , and outer sphere reorganization energies, λ_{os} ($\lambda = \lambda_{is} + \lambda_{os}$). λ_{is} is the relaxation energies for the complex, while λ_{os} accounts for the required energy to reorganize solvent distribution surrounding the complex. λ_{is} has the precursor contribution, λ_{is1} , and the products contribution, λ_{is2} ($\lambda_{is} = \lambda_{is1} + \lambda_{is2}$). λ_{is1} is the difference between the energy of products in their ground state at the precursors geometry, $E(\text{Prod})_{\text{PRE}}$, and the energy of products at their ground state optimized geometry, $E(\text{Prod})_{\text{OPT}}$ (Eq. 7). And λ_{is2} is the difference between the energy of

precursors in their ground state at the products geometry, $E(\text{Pre})_{\text{PROD}}$, and the energy of precursors at their ground state optimized geometry, $E(\text{Pre})_{\text{OPT}}$ (Eq. 8) (see Figure 1).

$$\lambda_{is1} = E(\text{Prod})_{\text{PRE}} - E(\text{Prod})_{\text{OPT}} \quad (7)$$

$$\lambda_{is2} = E(\text{Pre})_{\text{PROD}} - E(\text{Pre})_{\text{OPT}} \quad (8)$$

Meanwhile, the λ_{os} for continuum solvent models is given by:

$$\lambda_{os} = (\Delta q)^2 \left(\frac{1}{2r_1} + \frac{1}{2r_2} - \frac{1}{R} \right) \left(\frac{1}{D_{op}} - \frac{1}{\epsilon_s} \right) \quad (9)$$

where Δq is the charge transferred, r_1 and r_2 are the effective radii of the precursor molecules, R is the effective radius of the whole precursor complex and ϵ_s and D_{op} are the static and high frequency (optical) dielectric constants of the solvent. Radii are expressed in angstroms and, in our case, the charge transferred is equal to 1 and ϵ_s and D_{op} for acetonitrile are 35.688 and 1.801, respectively. The final λ_{os} value is given in eV.

The self-interaction error (SIE) intrinsic in density-functional theory has also been taken into account. SIE in DFT is the consequence of the fact that the residual self-repulsion in the Coulombic term of the energy functional is not totally cancelled by the exchange part of the functional.^{47,48} The SIE artificially stabilizes delocalized states, since delocalization reduces the self-repulsion.⁴⁹ Siegbahn *et al.* proposed a simple approach to measure the magnitude of the SIE effects in systems composed of a catalytic transition metal complex and a substrate molecule.⁵⁰ Their approach is based on the comparison of electronic spin density and energy of *a priori* two quasi-equivalent DFT structures: i) the localized states of the catalyst and substrate at infinite distance obtained from two different calculations; ii) the states obtained from a single calculation of the catalyst and substrate separated by a very long distance (e.g.

60 Å). The only difference between both types of calculations should be the small Coulomb interaction between the catalyst and the substrate at 60 Å. If the latter DFT calculation leads to different electronic spin density and lower energy than the former (after removing the effect of the Coulomb interaction), the DFT calculation of such catalyst-substrate complex suffers SIE effects. On the contrary, if both calculations lead to the same electronic spin density and energy, there are no evidences of SIE effects on the catalyst-substrate complex. In this paper we have used this approach to measure the possible SIE effects of the compounds studied here (see SI for more details).

The AHP may involve different spin states. In our work, we analyzed the doublet, quartet, and sextuplet potential energy surfaces (PESs). Superscripts in the labels of the different species along the reaction coordinate refer to their spin multiplicity; 2, 4, and 6 stand for doublet, quartet and sextuplet, respectively. The relative spin state energies of UB3LYP/6-311G(d,p)~SDD structures have been checked at UOPBE/6-311G(d,p)~SDD level of theory (see Tables S4 and S5). Previous validation studies have shown the validity of the OPBE functional for the spin-state splittings of iron complexes.⁵¹⁻⁵⁴ The comparison between UB3LYP and UOPBE spin ground states indicates that same qualitative pictures are obtained with the two functionals. The same conclusion was drawn by de Visser et al. when comparing the spin state splittings obtained using the UB3LYP, UBLYP, UB3PW91, and TPSS functionals.⁵⁵ For this reason, we will focus on the UB3LYP results only.

For the cases where the energy surfaces of two spin multiplicities were close in energy and the obtained spin crossing was reliable, the minimum energy crossing

points (MECPs) were optimized and evaluated using Gaussian 09 together with the code developed by Harvey et al.⁵⁶

III. Results and discussion






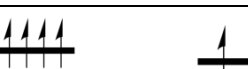
1. The electronic structure and stability of the iron-bishydroxo intermediate (**B** or **C**) formed after C–H bond breakage

The main difference between all pathways suggested in Scheme 1 lies on the stability and the electronic structure of the intermediate species that are formed after substrate C–H breakage by the $\text{Fe}^{\text{V}}(\text{O})(\text{OH})$ species (**A**): **B/R**[•] (**I_{rad}**) or **C/R**⁺ (**I_{cat}**). As explained above the examples reported in the literature suggest either: i) a highly asynchronous concerted mechanism for alkane hydroxylation (Path *b* in Scheme 1) without the existence of an intermediate; or ii) the rebound mechanism through a **R**[•]/**B** intermediate (Path *a* in Scheme 1). Nevertheless, in this work several **R**⁺/**C** intermediates have been optimized using different theoretical models. Furthermore, in most of the cases they are even thermodynamically more stable than their **I_{rad}** counterparts. These results suggest that the third pathway labeled as *c* in Scheme 2 may be also possible.

Table 1 summarizes the relative ΔG_{soln} stabilities of **I_{rad}** and **I_{cat}** intermediates at the three different spin states studied and for all analyzed substrates, namely, methane, ethane, cyclohexane, and 2,3-dimethylbutane. For each total spin state and iron oxidation state, only the most stable electronic configuration has been studied. The results show that the relative stability of methane intermediates is clearly different from that of other substrates. Most stable methane intermediates have the **R**[•]/**B** electronic structure for each of the three spin multiplicities studied. Indeed the methyl

cation/C form could not be optimized. On the contrary, for all other substrates, the most stable iron-bishydroxo structure is **C** with R^+ . The $I_{\text{rad}}-I_{\text{cat}}$ energy difference linearly correlates with the ionization energies (IE) of the substrate (see Figs. S9 and S10), which can be used to predict the relative stability of the two intermediates. Obviously, the correlation is even better if the IE of substrates are replaced by the IE of the radical alkyls (see Fig. S8 and below for further discussion).

Table 1. Relative Gibbs Energies (ΔG_{solv}) (kcal/mol) for radical and cation iron-bishydroxo catalyst intermediates for different spin multiplicities ($\mathbf{B} = \text{Fe}^{\text{IV}}(\text{OH})_2$; $R^\bullet =$ radical substrate; $I_{\text{rad}} = \mathbf{B}/R^\bullet$. $\mathbf{C} = \text{Fe}^{\text{III}}(\text{OH})_2$; $R^+ =$ cationic substrate; $I_{\text{cat}} = \mathbf{C}/R^+$).

UB3LYP-D2-SMD			substrates / ΔG_{solv} (kcal/mol)			
S	electronic configuration		methane	ethane	cyclohexane	2,3-DMB
	iron	substrate				
1/2	I_{cat} C		- ^a	9.66	10.38	- ^a
	I_{rad} B		0.00	8.86	23.28	- ^a
3/2	I_{cat} C		- ^a	9.34	9.52	10.52
	I_{rad} B		1.12	9.75	22.70	34.55
5/2	I_{cat} C		- ^a	0.00	0.00	0.00
	I_{rad} B		6.55	- ^a	- ^a	- ^a

^aWe were unable to optimize the intermediate in this particular electronic configuration.

Table 2 lists the relative ΔG_{solv} stabilities of I_{rad} and I_{cat} intermediates when considering the substrate and the catalyst separated by an infinite distance. Thus, it

presents the relative Gibbs energies of all possible combinations between the radical with $S=1/2$ (cationic with $S=0$) substrate and the $S=0$, $S=1$, and $S=2$ spin states of the **B** species ($S=1/2$, $S=3/2$, and $S=5/2$ spin states of the **C** species). Only the most stable \mathbf{I}_{rad} combinations shown in Table 2 were optimized as \mathbf{I}_{rad} intermediates (Table 1). In agreement with the results in Table 1, the data presented in Table 2 indicates that while methane has an \mathbf{I}_{rad} form as the lowest energy state, for all other substrates the \mathbf{I}_{cat} represents the lowest energy structure. The simple model used in Table 2 does not take into account the coupling between the substrate and the iron species. However, the approximate values of Table 2 are useful to offer an explanation on the relative Gibbs energies for the different intermediates at the different spin states. For instance, the results of Table 2 for methane point out that for $S=1/2$ the lowest-lying electronic state corresponds to the antiferromagnetic coupling of the methyl radical and the $S=1$ **B** species, whereas the methyl radical/ $S=0$ **B** or methyl cation/ $S=1/2$ **C** electronic states are more than 10 kcal/mol higher in energy.

Tables 1 and 2 show that for \mathbf{I}_{cat} the most stable multiplicity is always sextuplet, while for \mathbf{I}_{rad} intermediates the lowest-lying energy structures involve always a $S=1$ **B** moiety. For the latter, energies between antiferromagnetic and ferromagnetic equivalent species have always close values indicating a weak spin coupling between the unpaired electrons of the two fragments (see \mathbf{I}_{rad} species with total spin equals to $S=1/2$ and $S=3/2$ in Table 1). With the exception of methane, sextuplet multiplicity gives always the most stable \mathbf{I}_{cat} , due in part to the extra stability given by the half-filled d shell of the iron center. On the contrary, geometry optimization of the sextuplet radical states, which are given by a ferromagnetic coupling between \mathbf{R}^{\bullet} and the $S=2$ **B** catalyst, yields directly to alcohol products without the presence of a stable

intermediate. Furthermore, results of Table 2 indicate that the doublet and quadruplet I_{rad} are for all the substrates more stable than the sextuplet.

Table 2. Relative Gibbs energies (ΔG_{solv}) in kcal/mol for several radical and cation iron-bishydroxo catalyst electronic configurations, evaluated considering catalyst and substrate separated at infinite distance. Values in parenthesis correspond to Gibbs energy differences within the same multiplicity species ($\mathbf{B} = \text{Fe}^{\text{IV}}(\text{OH})_2$; \mathbf{R}^\bullet = radical substrate; $\mathbf{I}_{\text{rad}} = \mathbf{B}/\mathbf{R}^\bullet$; $\mathbf{C} = \text{Fe}^{\text{III}}(\text{OH})_2$; \mathbf{R}^+ = cationic substrate; $\mathbf{I}_{\text{cat}} = \mathbf{C}/\mathbf{R}^+$).

UB3LYP-D2-SMD			substrates / ΔG_{solv} (kcal/mol)			
S	iron configuration	substrate configuration	methane	ethane	cyclohexane	2,3-DMB
	I_{cat}	$\mathbf{C} \uparrow$ $\mathbf{R}^+ \text{---}$	26.65 (26.65)	10.37 (0.00)	10.37 (0.00)	10.37 (0.00)
1/2	I_{rad}	$\mathbf{B} \text{---}$ $\mathbf{R}^\bullet \uparrow$	11.85 (11.85)	25.02 (14.64)	37.81 (27.43)	48.89 (38.51)
	I_{rad}	$\mathbf{B} \uparrow\uparrow$ $\mathbf{R}^\bullet \uparrow\downarrow$	0.00 (0.00)	13.16 (2.79)	25.95 (15.58)	37.03 (26.66)
3/2	I_{cat}	$\mathbf{C} \uparrow\uparrow\uparrow$ $\mathbf{R}^+ \text{---}$	26.61 (26.61)	10.34 (0.00)	10.34 (0.00)	10.34 (0.00)
	I_{rad}	$\mathbf{B} \uparrow\uparrow$ $\mathbf{R}^\bullet \uparrow$	0.00 (0.00)	13.16 (2.83)	25.95 (15.62)	37.03 (26.70)
	I_{rad}	$\mathbf{B} \uparrow\uparrow\uparrow\uparrow$ $\mathbf{R}^\bullet \uparrow\downarrow$	5.66 (5.66)	18.82 (8.49)	31.61 (21.28)	42.70 (32.36)
5/2	I_{cat}	$\mathbf{C} \uparrow\uparrow\uparrow\uparrow\uparrow\uparrow$ $\mathbf{R}^+ \text{---}$	16.27 (10.61)	0.00 (0.00)	0.00 (0.00)	0.00 (0.00)
	I_{rad}	$\mathbf{B} \uparrow\uparrow\uparrow\uparrow$ $\mathbf{R}^\bullet \uparrow$	5.66 (0.00)	18.82 (18.82)	31.61 (31.61)	42.70 (42.70)

As a general trend, I_{cat} stabilization with respect to its I_{rad} counterpart ($\Delta G_{\text{solv}}^{I_{\text{rad}}} - \Delta G_{\text{solv}}^{I_{\text{cat}}}$) increases when the number of carbons attached to the carbon that suffers the HAT increases (see Table 2). Thus, the sextuplet cationic ethyl, cyclohexyl, and 2,3-

DMB/**B** intermediates are, respectively, 13.2 kcal/mol, 26.0 kcal/mol, and 37.0 kcal/mol more stable than the lowest energy **I_{rad}** intermediates, while **I_{rad}** is favored over cationic methyl/**B** by 16.3 kcal/mol. This can be easily predicted just from the ionization energy of **R[•]** (IE_{subst}) and the electron affinity of the **B** moiety (EA_{cat}) (see Tables S1 and S2). For all the studied substrates but methane the electron transfer process is thermodynamically favorable in solution (i.e. $IE_{\text{subst}} - EA_{\text{cat}} < 0$).

In summary, the results obtained analyzing all possible electronic states of the intermediates indicate that the new proposed mechanism c of Scheme 2 could be the most favorable for C–H oxidation at primary, secondary, or tertiary carbon atoms.

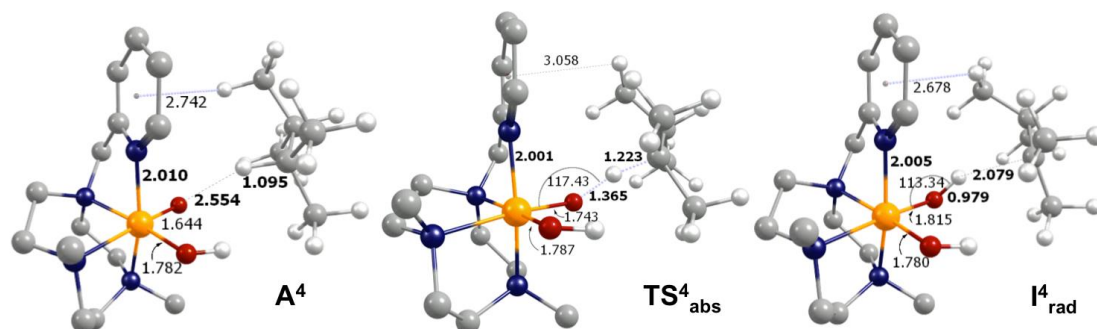
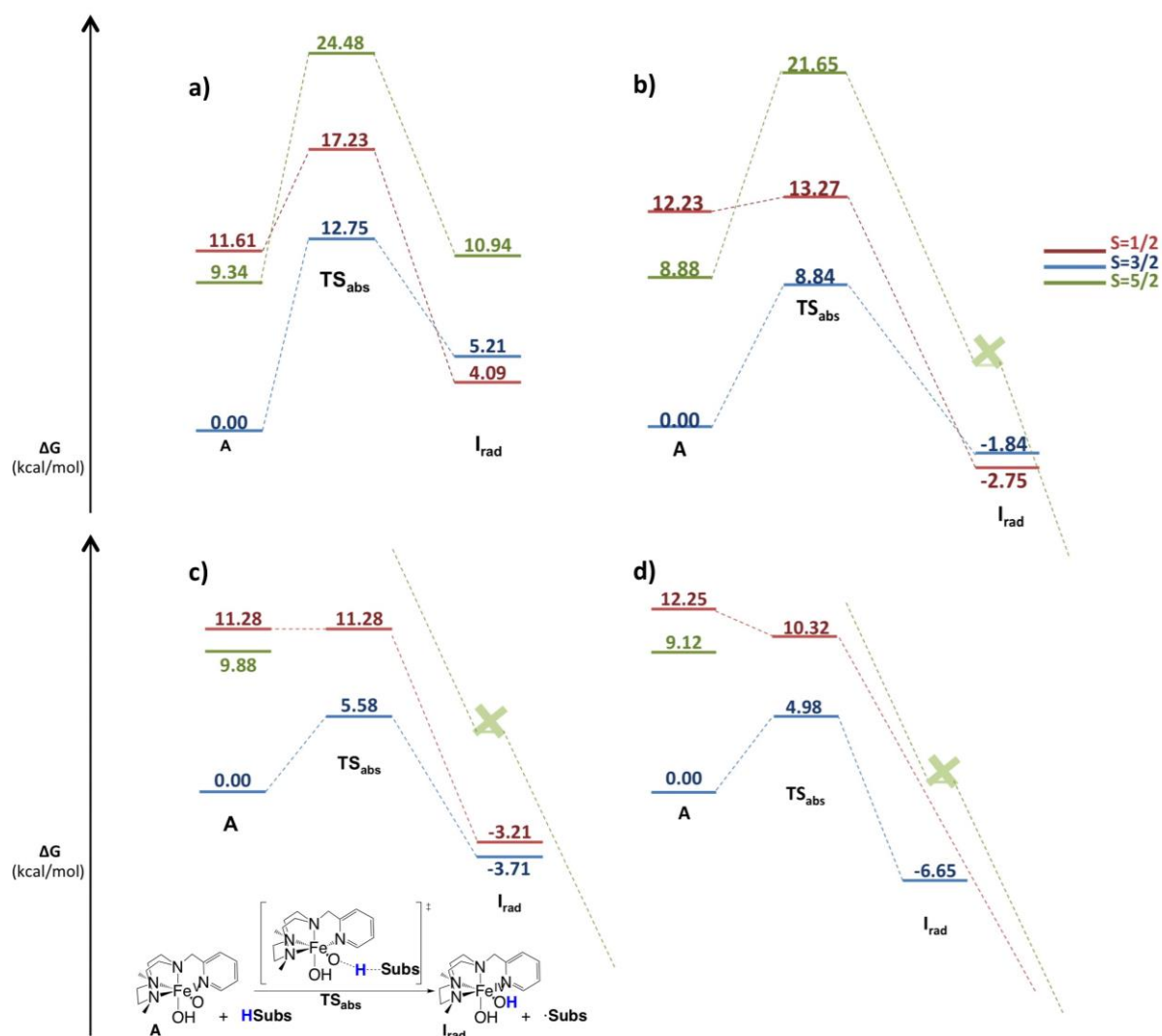


Figure 2. (Top) Gibbs energy profiles in solution (ΔG_{soln}) of the HAT step for (a) methane, (b) ethane, (c) cyclohexane, and (d) 2,3-DMB [$\text{kcal}\cdot\text{mol}^{-1}$]. Red, blue, and green profiles correspond to doublet, quartet, and sextuplet multiplicities, respectively. (Bottom) Structures of the HAT process for 2,3-DMB substrate in the ground state ($S=3/2$). Selected distances and angles are indicated in angstroms (\AA) and in degrees ($^\circ$), respectively. C atoms are represented in grey, N in blue, O in red, Fe in orange, and H in white. Hydrogen atoms of the PyTACN ligand have been omitted for clarity.

2. Mechanistic study of the Alkane Hydroxylation Process (AHP)

2.a. Hydrogen atom transfer (HAT) process. $[\text{Fe}^{\text{V}}(\text{O})(\text{OH})(\text{PyTACN})]^{2+}$ has been proposed as the active species in alkane²²⁻²⁴ and water⁵⁷⁻⁵⁹ oxidation. Moreover, its generation and its reaction with olefins has been proved by variable-temperature mass spectroscopy and DFT calculations.⁶⁰ The *cis* relative disposition of the oxo and hydroxo ligands gives two possible isomeric forms for $[\text{Fe}^{\text{V}}(\text{O})(\text{OH})(\text{PyTACN})]^{2+}$. The $[\text{Fe}^{\text{V}}(\text{O})(\text{OH})(\text{PyTACN})]^{2+}$ isomeric form that has the oxo group *trans* to a N-CH₃ moiety of the PyTACN ligand is the most stable one,²³ and consequently in the present mechanistic study it is assumed as the initial active species, **A**. To identify the key steps for the AHP, in this section we study the first step of the process, that is, the HAT process for all the studied substrates in acetonitrile solution (see Scheme 2).

An alternative to the HAT for the first step of the mechanism is a long-range electron transfer from the substrate to the high-valent $[\text{Fe}^{\text{V}}(\text{O})(\text{OH})(\text{PyTACN})]^{2+}$. This electron transfer first step mechanism was computationally determined by de Visser et al. as the most viable for $[\text{Fe}(\text{O})(\text{BQEN})(\text{NCCH}_3)]^{3+}$ (BQEN = N,N'-dimethyl-N,N'-bis(8-quinolyl)ethane-1,2-diamine), an iron(IV)-oxo ligand cation radical which has an extremely large electron affinity and therefore can abstract electrons from substrates.⁶¹ The same charge transfer first step mechanism was also found for Cpd I of P450⁶² and non heme iron(IV)-tosylimido species.⁶³ However, for $[\text{Fe}^{\text{V}}(\text{O})(\text{OH})(\text{PyTACN})]^{2+}$ the electron transfer is always far more endothermic than the HAT barrier, and then the electron transfer mechanism can be clearly ruled out (see Tables S7 and S8).

The Gibbs energy profiles for the HAT step of the four studied substrates are presented in Figure 2. The ground state of the initial active $\text{Fe}^{\text{V}}(\text{O})(\text{OH})$ species (\mathbf{A}^4) and HAT transition states ($\mathbf{TS}_{\text{abs}}^4$) are quartet spin states for all substrates, while $S=1/2$ and $S=5/2$ excited spin states are, at least, 4.5 kcal/mol higher in energy. The first excited state of $\text{Fe}^{\text{V}}(\text{O})(\text{OH})$ species is the sextuplet state and the second has a doublet spin state configuration. However, the opposite is true for the TS of the hydrogen abstraction. The inclusion of spin contamination, thermal, and entropy corrections have a key effect on the relative energy of the different spin states of the intermediates and transition states species (see Table S4). For cyclohexane, the calculated kinetic isotopic effect (KIE) for $\mathbf{TS}_{\text{abs}}^4$ using the classical transition state theory expressions is 4.9, in very good agreement with the experimental $\text{KIE}=4.3$.²³

Spin population analysis of \mathbf{A}^2 and \mathbf{A}^4 reveals two unpaired electrons on the iron and one unpaired electron on the oxo ligand antiferromagnetically or ferromagnetically coupled, respectively (See Table S3). The presence of this antiferromagnetic coupling translates into an important spin contamination correction in the unrestricted calculation of \mathbf{A}^2 . The electronic distribution for \mathbf{A}^6 is clearly different and shows three unpaired electrons on iron, a partial unpaired electron on the oxo ligand and almost an unpaired electron centered on the nitrogen atom of the pyridine group.

Our results show that HAT Gibbs energy barriers (ΔG^\ddagger) decrease when the number of carbon atoms bound to the C–H group that suffers the hydrogen abstraction increases. The same trend is found for the Gibbs reaction energies (ΔG_{reac}). $\Delta G_{\mathbf{A} \rightarrow \text{Irad}}$ becomes more exergonic when the number of carbons bound to the C that suffers

hydrogen abstraction increases. Then, whereas the HAT step for methane is endergonic (4.1 kcal/mol), for ethane, cyclohexane, and 2,3-DMB, the HAT process is exergonic by -2.8 kcal/mol, -3.7 kcal/mol, and -6.7 kcal/mol, respectively. And in agreement with the Bell-Evans-Polanyi principle, the hydrogen abstraction Gibbs energy barrier evolves from 12.8 kcal/mol for methane to 8.8, 5.6, and 5.0 kcal/mol for ethane, cyclohexane, and 2,3-DMB, respectively. Moreover, the HAT Gibbs energy barriers (ΔG^\ddagger) also concur with the strength of the broken C–H bond: the highest ΔG^\ddagger for the strongest C–H bond of methane, and then a lower ΔG^\ddagger for ethane, cyclohexane, and 2,3-DMB, respectively. The binding dissociation energy of the C–H bond is in part determined by the free radical stability that follows the order methyl < primary < secondary < tertiary.⁶⁴ As it was previously shown by de Visser *et al.*,^{65–67} the HAT energy barriers of the different substrates correlates linearly with the C–H bond dissociation energy (BDE_{C-H}) of the substrate abstracted hydrogen (see Figs. S6 and S7). Furthermore, the HAT energy barriers also show a good linear correlation with IEs of the substrates (see Fig. S5). The larger the IE, the higher the HAT barrier.

In addition, our calculations also show a clear relation between the HAT energy barrier and the TS_{abs} geometric parameters (see Figure 3 and Table S5). The longer (shorter) the C–H (O–H) bond distance in the TS_{abs} , the higher the HAT Gibbs energy barrier, thus suggesting a “late” transition state for higher barriers, in agreement with the predictions of the Hammond postulate. Hence, methane has the largest C–H distance and the shortest H–O distance for TS_{abs} structures (*late* transition state) whereas 2,3-DMB has the shortest C–H distance and the largest H–O distance among the different TS_{abs} structures. The HAT barrier show very good linear correlations with respect to the O–H bond distance and C–H bond distance of the TS_{abs} structures

(see Figs. S1 and S2). Furthermore, as it is shown in Figures S3 and S4, the HAT barriers also correlate with the imaginary frequencies and the spin density of the C bonded to the abstracted hydrogen of the TS_{abs} . The HAT barrier increases when the absolute values of the imaginary frequency and C spin density increase. A high value of the C spin density indicates a late HAT transition state.

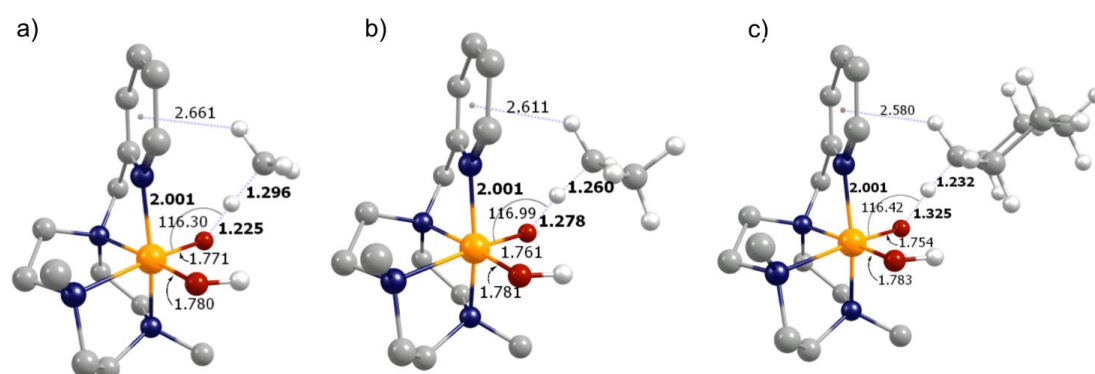
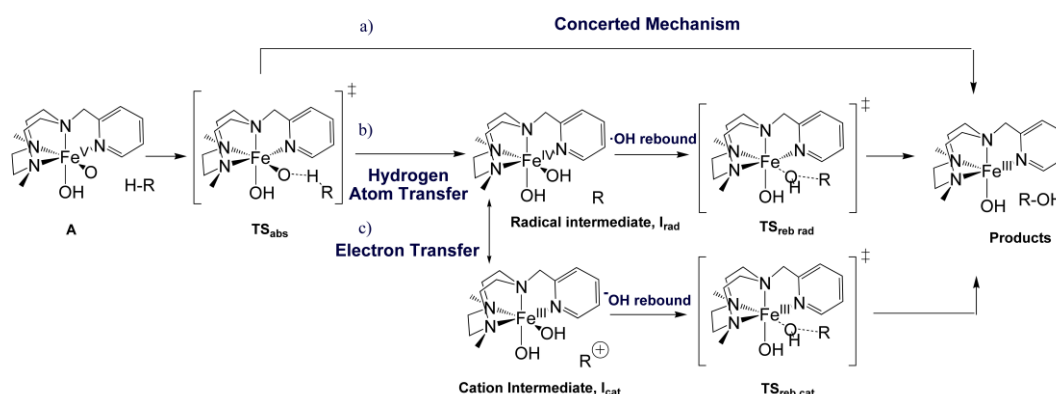


Figure 3. TS_{abs} structures in solution at $S=3/2$ for (a) methane, (b) ethane, and (c) cyclohexane, TS_{abs}^4 . Distances in Å and angles in degrees. C atoms are represented in grey, N in blue, O in red, Fe in orange, and H in white. Hydrogen atoms of the PyTACN ligand have been omitted for clarity.

TS_{abs} structures present a Fe-O-H angle of 108-117° for all studied multiplicities and substrates (see Figure 3). Thus, following Solomon and Neese terminology,^{68,69} the reaction proceeds via a π -channel with an orientation of the substrate that enhances the orbital overlap without increasing too much the Pauli repulsion. For quadruplet multiplicity, the results found are in agreement with the most-favorable π -channel hydrogen abstraction processes detected for iron(IV)-oxo moieties in the triplet state. Although we have also searched the linear σ -channel HAT transition state for the quadruplet and sextuplet states, all optimizations lead to the angular π -channel for the TS of the hydrogen abstraction. This scenario is in contrast with HAT reactions by $S=1$ $\text{Fe}^{\text{IV}}\text{O}$ complexes, that can occur both via a σ - and a π -paths.⁷⁰ The

presence of a CH/ π interaction⁷¹ between all substrates and the pyridine ring of $[\text{Fe}^{\text{V}}(\text{O})(\text{OH})(\text{PyTACN})]^{2+}$ complex favors the substrate orientation that triggers the π -channel for the hydrogen abstraction processes.

Scheme 3. The three proposed mechanisms for alkane hydroxylation processes catalyzed by $[\text{Fe}^{\text{V}}(\text{O})(\text{OH})(\text{PyTACN})]^{2+}$.

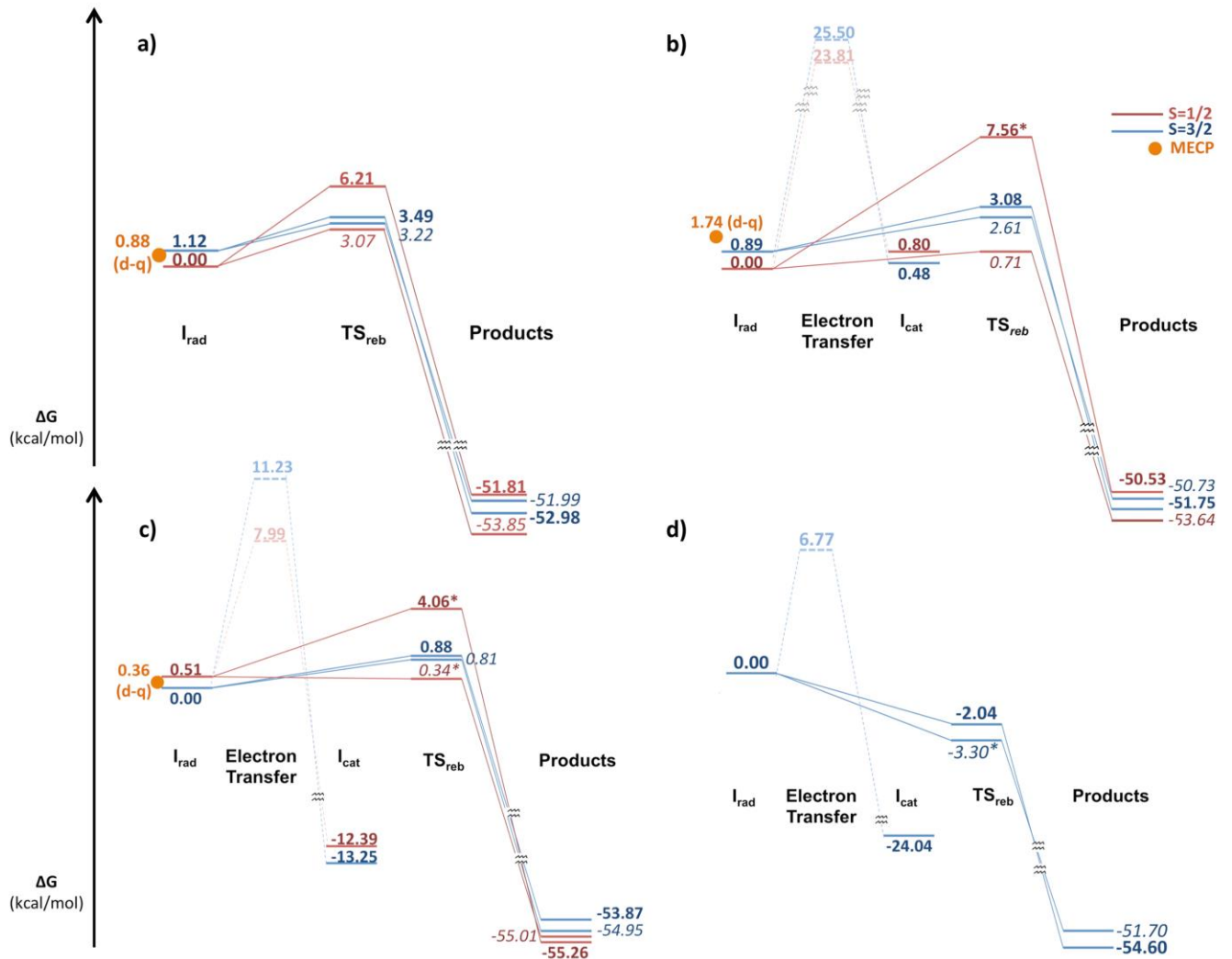


IRC calculations were done for TS_{abs} in order to ensure connection with the active species **A** and the next intermediate (I_{rad} or I_{cat}). The IRC calculations show that TS_{abs}^4 always leads to an I_{rad} intermediate (see Figure 2). Thus, in acetonitrile solution, the studied hydroxylation reactions at the $S=3/2$ ground state are stepwise because the HAT does not lead directly to products, but instead an I_{rad} intermediate is found. However, for $S=5/2$ state of ethane, cyclohexane, and 2,3-DMB and the $S=1/2$ state for 2,3-DMB, TS_{abs} directly connects with the final products. Thus, for these excited states, the mechanism can be defined as a highly asynchronous concerted process. Although for all the substrates but methane I_{cat} is more stable than I_{rad} , our calculations show that the first step of the mechanism is always hydrogen abstraction instead of a hydride abstraction. Thereby, IRC calculations discard path *c* suggested in Scheme 2. To achieve the more stable I_{cat} , an electron transfer, ET, process through a

second step would be necessary and then the proposed mechanisms for AHP for $[\text{Fe}^{\text{V}}(\text{O})(\text{OH})(\text{PyTACN})]^{2+}$ could be rewritten as shown in Scheme 3.

2.b. Electron transfer versus rebound (hydroxyl ligand transfer). As explained in the previous section, the ground state TS_{abs}^4 always leads to \mathbf{I}_{rad} . Nevertheless, after the HAT step, \mathbf{I}_{rad} can evolve to the alcohol product through a hydroxyl radical transfer (rebound step path *b* in Scheme 3) or can be followed by an ET step to \mathbf{I}_{cat} (path *c* in Scheme 3). In this section the competition between the OH radical rebound process and the ET step is evaluated.

The ET step has been studied for the two most stable multiplicities of \mathbf{I}_{rad} of ethane and cyclohexane, that is quadruplet and doublet multiplicities. For 2,3-DMB, only quadruplet \mathbf{I}_{rad} has been found. For methane \mathbf{I}_{cat} is less stable than \mathbf{I}_{rad} and the ET was discarded. Marcus theory (see Computational Details) has been used to analyze the kinetics of the ET processes. The kinetics of hydroxyl radical rebound step was determined by optimizing the corresponding TS. Gibbs energy profiles of the ET and OH-rebound pathways are shown in Figure 4 and the corresponding structures for the ethane case are depicted in Figure 5.



Hydroxyl ligand transfer

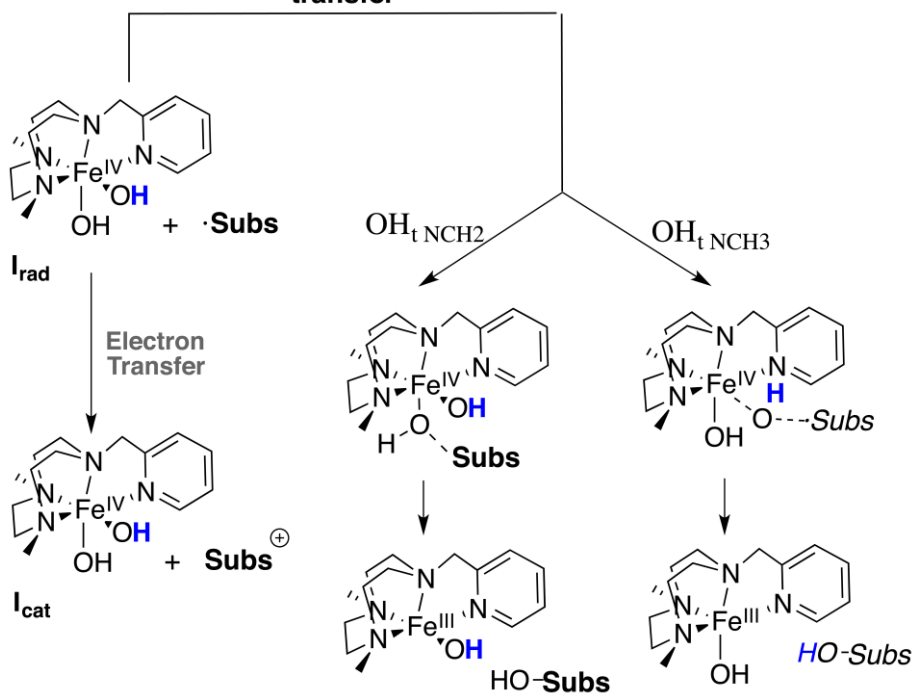


Figure 4. (Top) Gibbs energy profiles (in kcal/mol) in acetonitrile solution (ΔG_{solv}) of the ET and the hydroxyl ligand transfer for (a) methane, (b) ethane, (c) cyclohexane, and (d) 2,3-DMB catalyzed by $[\text{Fe}^{\text{IV}}(\text{OH})(\text{OH})(\text{PyTACN})]^{2+}$. Red profiles correspond to doublet and blue ones to quartet multiplicity states. Values in *italics* represent the $\text{OH}_{\text{t NCH}_2}$ ligand transfer and **bold** values represent the $\text{OH}_{\text{t NCH}_3}$ ligand transfer. The values marked with an * are approximated upper bound solutions obtained by scanning the C–O bond in linear transits from \mathbf{I}_{rad} to products. **(Bottom)** Reaction mechanisms analyzed in the Gibbs energy profiles.

For \mathbf{A} and \mathbf{TS}_{abs} , the $S=3/2$ spin state is the ground state for all substrates. But for \mathbf{I}_{rad} , whereas the quadruplet is still the ground state for cyclohexane and 2,3-DMB, for methane and ethane the ground state is $S=1/2$. The doublet-quadruplet (d-q) minimum-energy crossing point (MECP) for methane, ethane, and cyclohexane \mathbf{I}_{rad} intermediates is clearly lower in energy than the quadruplet barriers for ET and OH-rebound. However, the major change between the doublet and quadruplet spin density is located in the substrate carbon radical, and then the d-q spin-crossing is likely to be not allowed due to the small spin-coupling term of the dipole moment of the transition integral. Then we have studied the ET and OH-rebound on doublet and quadruplet multiplicities. Moreover, the TSs for the hydroxyl rebound in the two -OH groups of the $[\text{Fe}^{\text{IV}}(\text{OH})_2(\text{PyTACN})]^{2+}$ structure have also been studied. OH groups are labeled as $\text{OH}_{\text{t NCH}_2}$ and $\text{OH}_{\text{t NCH}_3}$. $\text{OH}_{\text{t NCH}_2}$ is the OH that has an $\text{N}-(\text{CH}_2)_3-$ group in *trans* (and it is the initial oxo group), whereas $\text{OH}_{\text{t NCH}_3}$ has an $\text{N}-(\text{CH}_2)_2(\text{CH}_3)-$ group in *trans*.

In Figures 4b-d the ET processes are represented in pale dashed lines, while the two different possible OH rebounds are represented in bold and italics. For all substrates, Figures 4a-d clearly show that the OH rebound is kinetically more favorable than the ET. For ethane, OH rebound barriers are in between **1.2 and 1.5 kcal·mol⁻¹** while ET activation energies range from 23.8 to 25.5 kcal·mol⁻¹. It is worth noting that the

$C_2H_5^+$ moiety in I_{cat} has the H^+ bridge C_{2v} conformation, which is the most stable for the free ethyl cation at the B3LYP and CCSD levels of theory (see Figure 5).⁷² For cyclohexane, OH rebound barriers are in the interval from 0.8 to 0.9 kcal·mol⁻¹ while ET activation energy are in between 8.0 and 11.2 kcal·mol⁻¹. Finally, 2,3-DMB has a barrierless OH rebound while the ET process has an energetic cost of 6.8 kcal·mol⁻¹. Again, lower activation barriers correspond to more exergonic products.

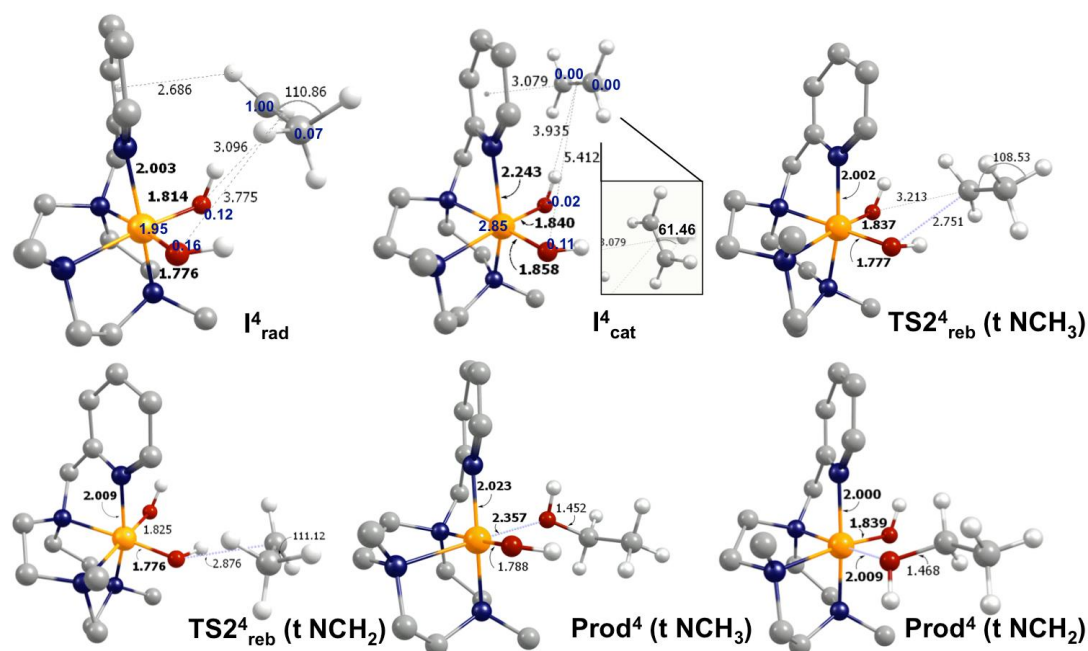


Figure 5. Structures involved in the ET and the hydroxyl ligand transfer processes for ethane. Selected distances and angles are indicated in angstroms (Å) and in degrees (°), respectively. Selected spin densities (in electrons) are given in blue. C atoms are represented in grey, N in blue, O in red, Fe in orange and H in white. Hydrogen atoms of the PyTACN ligand have been omitted for clarity.

It has been experimentally proved on the basis of isotopic labeling and product analyses that the radical is short living and does not diffuse freely in the alkane hydroxylation reaction catalyzed by the $[Fe^V(O)(OH)(PyTACN)]^{2+}$ complex.²²⁻²⁴ Therefore, in this paper the dissociation mechanism has not been studied.

To summarize, electron transfer and rebound Gibbs energy barriers share the same behavior: they decrease when the number of C atoms bonded to the radical carbon increases. Indeed both processes account for a $1e^-$ reduction from Fe^{IV} to Fe^{III} and an oxidation of the substrate. The ET is a pure electron transfer, whereas the rebound process entails oxygenation of the substrate to form an alcohol. Thus, in terms of the formal oxidation state of the iron center both reactions formally account for a similar process and share the same behavior (i.e. the barriers decrease from methane to 2,3-dimethylbutane), being the barriers for the rebound always lower than the ET barriers.

2.c. The complete alkane hydroxylation mechanism. From the results obtained in the two previous subsections it can be concluded that: i) AHP always goes through the general *rebound* mechanism (path *b* in Scheme 2); and ii) I_{cat} is never an intermediate of the AHP mechanism. The ground state profiles for methane, ethane, cyclohexane, and 2,3-DMB hydroxylation are represented in Figure 6. The ground state of the active initial species, $Fe^V(O)(OH)$, is always the quartet and the hydrogen abstraction also goes through this multiplicity (which has 3 unpaired electrons on the catalyst). The Gibbs energy profiles clearly show that the hydrogen abstraction process is the TOF-determining transition state (TDTS).⁷³ I_{rad} S=1/2 and S=3/2 states have similar Gibbs energies for all studied substrates since they have the same electron distribution (3 electrons on the catalyst: 2 in the iron d shell and one in the oxo moiety) with weak coupling with the substrate (ferromagnetic or antiferromagnetic). Then, I_{rad} ground state multiplicity varies between S=1/2 and S=3/2 depending on the substrate (doublet for methane and ethane and quartet for cyclohexane and 2,3-DMB).

The OH radical rebound (TS_{reb}) has been evaluated for doublet and quartet multiplicities for both isomeric positions despite the d-q spin crossing is likely to be

not allowed (see above). The rebound with the OH *trans* to NCH₂ is always the most favorable one and its ground state is again doublet for methane and ethane and quartet for cyclohexane and DMB, as for I_{rad}. The rebound with the hydroxyl *trans* to NCH₃ is less than one kcal/mol higher in energy than the rebound with the OH *trans* to the NCH₂ moiety, except for methane, where the difference is larger than 6 kcal/mol. Thus, the calculations show that the rebound with the OH *trans* to NCH₂ moiety is the most favorable one, although these results should be taken with some caution since energy differences between both rebounds are within the limits of precision of the used DFT approach. The final products with the alcohol formed fall down to sextuplet states.

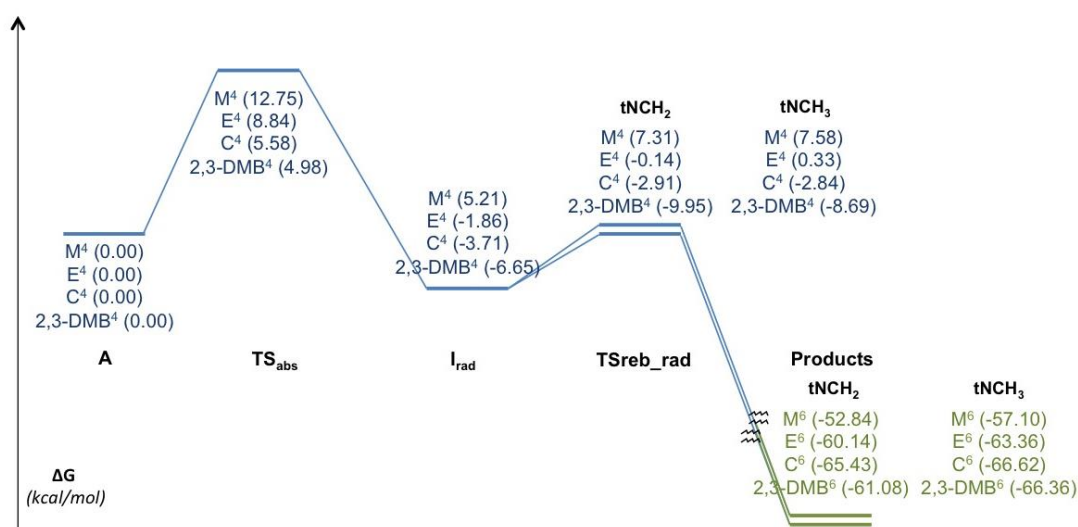


Figure 6. Gibbs energy (in kcal/mol) profiles for methane, M, ethane, E, cyclohexane, C, and 2,3-dimethylbutane, 2,3-DMB, hydroxylation processes. Only the ground state for each substrate and structure are represented. Red accounts for doublet, blue for quartet, and green for sextuplet ground states.

3. Comparison between gas-phase and solvent-phase mechanisms

As previously mentioned in the introduction, computational studies of the reaction mechanism for alkane oxidation processes catalyzed by Fe^VO do not present a clearly

established pathway for many substrates and catalysts. DFT equilibrium geometries of the intermediates and transition states of the proposed mechanisms are usually optimized at gas-phase. In some cases, the solvent-phase corrections are included through single-point solvent-phase corrections. Here we will show that the single-point calculations approach to include the solvent-phase effects is not always a good method to determine the reaction mechanism in solution and that the solvent-effects should also be included during the optimization of the equilibrium geometries. In the first part of this paper, depending on the substrate two different trends for the relative stability of the \mathbf{I}_{cat} and \mathbf{I}_{rad} intermediates have been observed in solution. While for methane the \mathbf{I}_{rad} structure is the most stable, for all the other alkane substrates \mathbf{I}_{cat} is the most stable form. To assess the reliability of the different approaches given by Eqs (3)-(5) (i.e. G_g , G_{g+corr} and G_{solv}) to describe AHP properly, one substrate of each group (methane and cyclohexane) has been studied computationally with the three methodologies.

We have also studied the electronic structure and stability of the iron-bishydroxo intermediates for methane and cyclohexane at gas-phase (G_g) and at gas-phase including single-point dispersion and acetonitrile solvent corrections (G_{g+corr}). The gas-phase Gibbs energy of all possible combinations between the radical (cationic) substrate and all possible multiplicities of the catalyst at infinite distance are listed in Tables S6 and S7. Comparison of these gas-phase (Table S6) and solvent-phase (Table 2) values show that the acetonitrile solution stabilizes \mathbf{I}_{rad} over the most stable \mathbf{I}_{cat} . The larger solvent stabilization of \mathbf{I}_{rad} as compared to \mathbf{I}_{cat} is caused by the localization of the +2 positive charge on the catalyst in the former intermediate. The solvent relative stabilization of \mathbf{I}_{rad} as compared to \mathbf{I}_{cat} increases when the size of the

substrate increases. However, the latter effect is smaller than the stabilization of \mathbf{I}_{cat} due to the reduction of IE_{subst} when the size of the substrate increases. As it is well-known the general stability of simple alkyl carbocations follows the trend tertiary > secondary > primary > methyl.⁷⁴ Finally, we want to note that when the single-point energy corrections for dispersion and solvent effects are added to the gas-phase values, the values obtained lead to the same conclusions than the results obtained in solution (see Table S7).

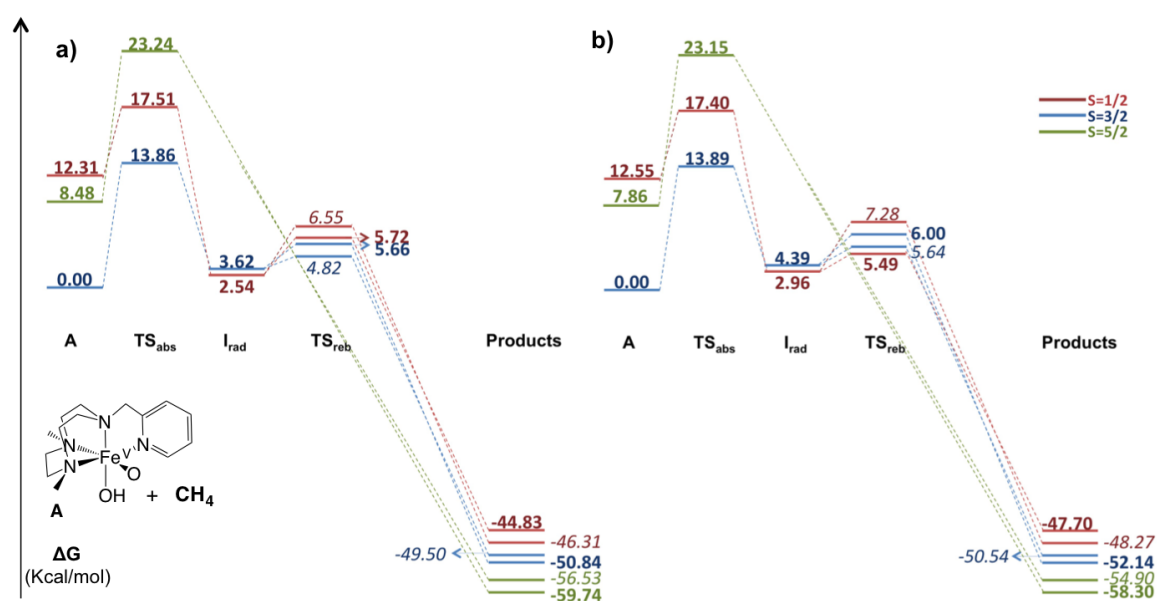


Figure 7. Gibbs energy profile in kcal/mol for the AHP of methane at gas-phase (G_g) (a) and at gas-phase including the dispersion and solvent corrections (G_{g+corr}) (b). Values in *italics* represent the $\text{OH}_{\text{tNCH}_2}$ ligand transfer and **bold** values represent the $\text{OH}_{\text{tNCH}_3}$ ligand transfer.

The effect of the coupling between the substrate and the catalyst has also been studied considering the whole intermediate (substrate + catalyst) (see Table S8). Again, gas-phase and solvent-phase results give the same general trends. However, a few key differences between solvent- and gas-phase intermediates appear here. In the gas-phase, unlike in solution, there are not stable \mathbf{I}_{cat} (\mathbf{I}_{rad}) intermediates for methane (cyclohexane). For these electronic states, optimizations at gas-phase lead directly to

the alcohol products without finding any stable intermediate. The observed differences already seem to indicate that i) gas-phase and solution reaction mechanisms can be different for a given substrate and ii) for two different substrates, the reaction mechanisms can differ even if they are computed in the same phase (gas or solution). This may explain the diversity of alkane hydroxylation reaction mechanisms found in the literature.^{23,25,29,30} For this reason, we studied the gas-phase hydroxylation mechanisms of methane and cyclohexane and we compared them with those obtained in solution.

For methane substrate, the AHP Gibbs energy profile obtained at gas-phase (Figure 7) is very similar to the one obtained in solution (Figures 2 and 4) with the exception of the sextuplet multiplicity state, for which the intermediate \mathbf{I}_{rad} cannot be optimized at gas-phase. Thus, although the G_{g+corr} approach introduces only part of the solvent effects, for the methane case, G_{g+corr} methodology gives a good semiquantitative description of the solvent-phase profile.

For cyclohexane, differences between G_g , G_{g+corr} , and G_{solv} profiles are qualitatively far more important than for methane. As it has already been mentioned, \mathbf{I}_{rad} for cyclohexane at gas-phase is not a stable minimum, and after the hydrogen abstraction the process yields directly to products (compare Fig. 8 with Figs. 2 and 4). The cationic intermediates \mathbf{I}_{cat} , which are stable minima at gas-phase, are not part of the mechanism reaction pathway. Thus, the difference in \mathbf{I}_{cat} stabilization between gas-phase and solvent clearly affects the reaction mechanism derived from Gibbs energy profiles. Whereas in solution the cyclohexane hydroxylation by $[\text{Fe}^{\text{V}}(\text{O})(\text{OH})(\text{PyTACN})]^{2+}$ catalyst follows a HAT + rebound stepwise mechanism, at gas-phase the cyclohexane hydroxylation mechanism is concerted and highly

asynchronous. Nevertheless, in both cases, the TOF-determining transition state (TDTS) is given by the HAT transition state. In this case, on the contrary to methane hydroxylation, G_{g+corr} approach turns to be an unreliable method to determine the solvent-phase mechanism.

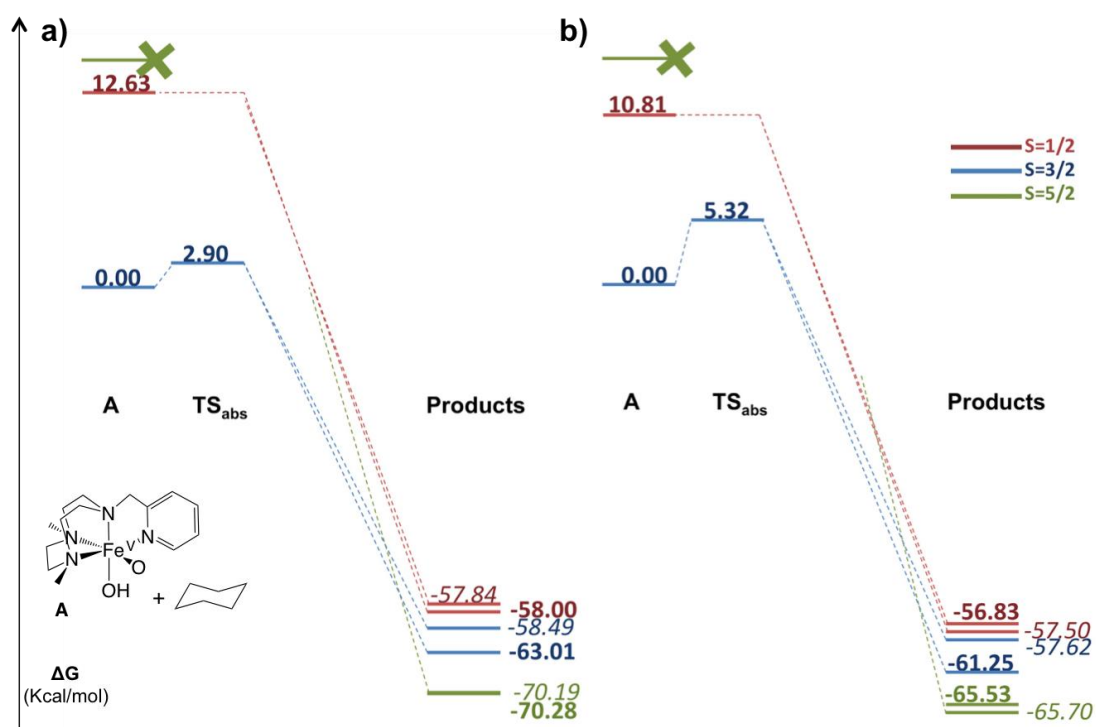


Figure 8. Gibbs energy profiles in kcal/mol for the AHP of cyclohexane at gas-phase (a) and at gas-phase including dispersion and solvent corrections (b). Values in *italics* represent products where the alcohol group comes from the OH_{tNCH_2} .

Another difference between cyclohexane hydroxylation Gibbs energy profiles at gas-phase and in solution is that while at gas-phase the S=3/2 products are more stable than S=1/2 products, the opposite is true in solution. Also here G_{g+corr} approach fails in describing the relative stability of these excited spin states in solution.

Finally, let us mention that in a recent DFT modeling of the C-H abstraction catalyzed by the non-heme $[N_4PyFe^{IV}O]^{2+}$ compound, Shaik et al. showed that for

this system the effects of the self-interaction error in DFT lead to an incorrect description of the hydroxylation mechanism.⁷⁵ Using the approach given by Siegbahn,⁵⁰ we have computed the SIE of all optimized radical intermediates, \mathbf{I}_{rad} , and cationic intermediates, \mathbf{I}_{cat} . Our check covers all substrates and more stable spin states for both gas- and solution-phase optimized structures. None of our optimized structures suffers significant SIE effects (see Tables S13-S18). Nevertheless, Shaik and coworkers paper and our work are perfectly complementary to describe how to achieve a proper description of the alkane hydroxylation mechanism by means of DFT. In the former case, a $\text{Fe}^{\text{IV}}\text{O}$ species is studied and removing the effects of the SIE is essential. Instead, in our work case, hydroxylation is mediated by a Fe^{VO} species, and SIE has no role. But in both works the utilization of gas-phase optimized structures is strongly discouraged.

IV. CONCLUSIONS

In this work, we have investigated with DFT methods the stereospecific hydroxylation of a series of alkanes (methane, ethane, cyclohexane, and 2,3-dimethylbutane) that occurs in the presence of $[\text{Fe}^{\text{II}}(\text{CH}_3\text{CN})_2(\text{PyTACN})]^{2+}$ species treated with excess of H_2O_2 in acetonitrile. Our computational results support the proposal that the mechanism for alkane hydroxylation processes takes place through high-valent $[\text{Fe}^{\text{V}}(\text{O})(\text{OH})(\text{PyTACN})]^+$ species. Furthermore, we have determined the key effects of the substrate and solvent in the hydroxylation mechanism. In acetonitrile solution, a stepwise mechanism that starts with a hydrogen atom transfer and follows with a hydroxyl radical rebound is determined for methane, ethane, cyclohexane, and 2,3-dimethylbutane. The same mechanism is valid for the gas-phase methane hydroxylation. On the contrary, gas-phase cyclohexane hydroxylation

evolves through a concerted and highly asynchronous mechanism. Namely, gas-phase \mathbf{I}_{rad} intermediates are not stabilized and the initial hydrogen atom transfer yields directly to the alcohol products. The differences between acetonitrile solution and gas-phase cyclohexane mechanisms can be attributed to the important stabilization by the acetonitrile solvent of \mathbf{I}_{rad} intermediate that has a 2+ charge in the catalyst and is neutral in the \mathbf{R}^{\bullet} moiety.

\mathbf{I}_{cat} structures are thermodynamically more stable than \mathbf{I}_{rad} intermediates for ethane, cyclohexane, and 2,3-dimethylbutane. However, IRC calculations and Marcus theory prove that the \mathbf{I}_{cat} species are not involved in the hydroxylation mechanism. Although the electron transfer barriers of the evolution of \mathbf{I}_{rad} to \mathbf{I}_{cat} are smaller than 26 kcal/mol, OH radical rebound barriers for \mathbf{I}_{rad} are always far lower. Thus, after the hydrogen abstraction the iron-bishydroxo intermediate goes to the alcohol products instead of evolving via an electron transfer process. For methane, \mathbf{I}_{rad} structures are more stable than \mathbf{I}_{cat} ones, and then the electron transfer process can be ruled out. Kinetics of the hydrogen atom transfer step is always energetically more demanding than the rebound step, being the former the rate-determining step.

In a previous work we showed that for the non-heme iron catalyst studied in this paper, ^{18}O -labeling experiments give an equal incorporation of oxygen from water and from peroxide in the final cyclohexanol products.²³ Taking into account that the mechanism in acetonitrile solvent is stepwise, in order to explain these labeling results the activation barriers of both the hydrogen atom transfer and the rebound steps should be very similar for the two *cis* active sites. In our previous work, some of us showed that this condition is fulfilled for the hydrogen atom transfer step. The results

presented here for cyclohexane substrate show that the hydroxyl rebounds barriers for the two –OH groups are nearly identical ($\Delta\Delta G^\ddagger$ of the hydroxyl ligand transfer between the two –OH groups of cyclohexane is less than 0.1 kcal/mol). Thus, the DFT profile for the hydroxylation of cyclohexane catalyzed by $[\text{Fe}^{\text{V}}(\text{O})(\text{OH})(\text{PyTACN})]^{2+}$ presented here is in agreement with the labeling results measured in our previous study. Furthermore, the clarification of the hydroxylation mechanism in acetonitrile solvent as stepwise is also key for the complete rationalization of the experimental ^{18}O incorporation yields that point that the incorporation of oxygen comes only (or mostly) from water or from the peroxide. In this case both the hydrogen atom transfer and the rebound steps should favor one of the two *cis* labile positions of $[\text{Fe}^{\text{V}}(\text{O})(\text{OH})(\text{PyTACN})]^{2+}$.

Finally, the calculation of minimum-energy crossing points between doublet and quartet potential energy surfaces for methane, ethane, and cyclohexane shows that the two-state reactivity (TSR) does not play a key role in the HAT step. For I_{rad} , the MECP studies show that the energetic cost of crossing from the quadruplet state to the doublet state is always lower than the energy needed to surmount the barriers of the rebound processes. However, the changes between the I_{rad}^2 and I_{rad}^4 spin densities occur in the radical carbon of the substrate, which implies a low spin-orbit coupling term for the spin crossing transition integral. Therefore, the rebound process evolves always through the $S=3/2$ spin state potential energy surface since the spin crossing is likely to be not allowed. For the 2,3-DMB hydroxylation, only the quartet state plays a role since the doublet Gibbs energy profile mechanism, which is concerted, is always much higher in energy.

ASSOCIATED CONTENT

Supporting Information. Ionization energies of the radical substrates (IE_{subs}), electron affinities of the **B** moiety (EA_{cat}), Mulliken spin population values of A_x complexes, UOPBE energy values for different spin states, gas-phase (G_g), and gas-phase including the dispersion and solvent corrections energy values (G_{g+corr}) for all the possible combinations between the radical (cationic) substrate and all possible multiplicities of the catalyst at infinite distance and also considering the optimized intermediate, and xyz coordinates for all the structures. This material is available free of charge via the Internet at <http://pubs.acs.org>.

AUTHOR INFORMATION

Corresponding Authors

* E-mail: miquel.sola@udg.edu, miquel.costas@udg.edu, josepm.luis@udg.edu.

ACKNOWLEDGMENTS

This work has been supported by Ministerio de Economía y Competitividad of Spain (Projects CTQ2014-54306-P, CTQ2014-52525-P, and CTQ2012-37420-C02-01, Ramón y Cajal contract to A.C., and grant No. BES-2012-052801 to V.P.), Generalitat de Catalunya (project numbers 2014SGR931, 2014SGR862, Xarxa de Referència en Química Teòrica i Computacional, and ICREA Academia prizes for M.S. and M.C.), the European Commission (ERC-2009-StG-239910 to M.C. and FP7-PEOPLE-2011-CIG-303522 to A.C.). and European Fund for Regional Development (FEDER grant UNGI10-4E-801).

REFERENCES

- (1) Company, A.; Gómez, L.; Costas, M. In *Alkane C-H Activation by Single-Site Metal Catalysis*; Perez, P. J., Ed.; Springer: Dordrecht, 2013; pp. 143–228.
- (2) Newhouse, T.; Baran, P. S. *Angew. Chem. Int. Ed.* **2011**, *50*, 3362–3374.
- (3) Ortiz De Montellano, P. R. *Chem. Rev.* **2010**, *110*, 932–948.
- (4) Kovaleva, E. G.; Lipscomb, J. D. *Nat. Chem. Biol.* **2008**, *4*, 186–193.
- (5) Costas, M.; Mehn, M. P.; Jensen, M. P.; Que, L. *Chem. Rev.* **2004**, *104*, 939–986.
- (6) Guengerich, F. P.; Munro, A. W. *J. Biol. Chem.* **2013**, *288*, 17065–17073.
- (7) White, M. C. Adding Aliphatic C-H Bond Oxidations to Synthesis. *Science*, 2012, *335*, 807–809.
- (8) Costas, M. *Coord. Chem. Rev.* **2011**, *255*, 2912–2932.
- (9) Que, L.; Tolman, W. B. *Nature* **2008**, *455*, 333–340.
- (10) Company, A.; Gómez, L.; Costas, M. *Focus Catal.* **2012**, *2012*, 8.
- (11) Bryliakov, K. P.; Talsi, E. P. *Coord. Chem. Rev.* **2014**, *276*, 73–96.
- (12) Ensing, B.; Buda, F.; Blöchl, P.; Baerends, E. J. *Angew. Chem. Int. Ed.* **2001**, *40*, 2893–2895.
- (13) Buda, F.; Ensing, B.; Gribnau, M. C.; Baerends, E. J. *Chem. Eur. J.* **2001**, *7*, 2775–2783.
- (14) Ensing, B.; Buda, F.; Baerends, E. J. *J. Phys. Chem. A* **2003**, *107*, 5722–5731.
- (15) McDonald, A. R.; Que, L. *Coord. Chem. Rev.* **2013**, *257*, 414–428.
- (16) Nam, W.; Lee, Y.-M.; Fukuzumi, S. *Acc. Chem. Res.* **2014**, *47*, 1146–1154.
- (17) Kaizer, J.; Klinker, E. J.; Oh, N. Y.; Rohde, J. U.; Song, W. J.; Stubna, A.; Kim, J.; Münck, E.; Nam, W.; Que, L. *J. Am. Chem. Soc.* **2004**, *126*, 472–473.
- (18) Krebs, C.; Galonić Fujimori, D.; Walsh, C. T.; Bollinger, J. M. *Acc. Chem. Res.* **2007**, *40*, 484–492.
- (19) De Visser, S. P. *J. Am. Chem. Soc.* **2006**, *128*, 9813–9824.

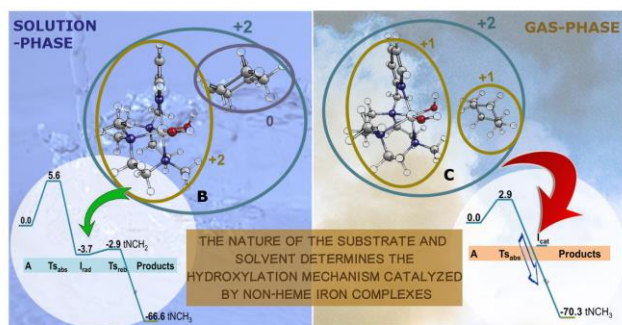
- (20) Hirao, H.; Kumar, D.; Que, L.; Shaik, S. *J. Am. Chem. Soc.* **2006**, *128*, 8590–8606.
- (21) Chen, K.; Que, L. *J. Am. Chem. Soc.* **2001**, *123*, 6327–6337.
- (22) Company, A.; Gómez, L.; Güell, M.; Ribas, X.; Luis, J. M.; Que, L.; Costas, M. *J. Am. Chem. Soc.* **2007**, *129*, 15766–15767.
- (23) Prat, I.; Company, A.; Postils, V.; Ribas, X.; Que, L.; Luis, J. M.; Costas, M. *Chem. Eur. J.* **2013**, *19*, 6724–6738.
- (24) Company, A.; Gómez, L.; Fontrodona, X.; Ribas, X.; Costas, M. *Chem. Eur. J.* **2008**, *14*, 5727–5731.
- (25) Bassan, A.; Blomberg, M. R. A.; Siegbahn, P. E. M.; Que, L. *Chem. Eur. J.* **2005**, *11*, 692–705.
- (26) Hitomi, Y.; Arakawa, K.; Funabiki, T.; Kodera, M. *Angew. Chem. Int. Ed.* **2012**, *51*, 3448–3452.
- (27) Tiago de Oliveira, F.; Chanda, A.; Banerjee, D.; Shan, X.; Mondal, S.; Que, L.; Bominaar, E. L.; Münck, E.; Collins, T. J. *Science* **2007**, *315*, 835–838.
- (28) Ghosh, M.; Singh, K. K.; Panda, C.; Weitz, A.; Hendrich, M. P.; Collins, T. J.; Dhar, B. B.; Gupta, S. S. *J. Am. Chem. Soc.* **2014**, *136*, 9524–9527.
- (29) Kwon, E.; Cho, K.-B.; Hong, S.; Nam, W. *Chem. Commun.* **2014**, *50*, 5572–5575.
- (30) Noack, H.; Siegbahn, P. E. M. *J. Biol. Inorg. Chem.* **2007**, *12*, 1151–1162.
- (31) Cho, K. Bin; Wu, X.; Lee, Y. M.; Kwon, Y. H.; Shaik, S.; Nam, W. *J. Am. Chem. Soc.* **2012**, *134*, 20222–20225.
- (32) Comba, P.; Maurer, M.; Vadivelu, P. *J. Phys. Chem. A* **2008**, *112*, 13028–13036.
- (33) Frisch, M. J.; Trucks, G. W.; Schlegel, H. B.; Scuseria, G. E.; Robb, M. A.; Cheeseman, J. R.; Scalmani, G.; Barone, V.; Mennucci, B.; Petersson, G. A.; Nakatsuji, H.; Caricato, M.; Li, X.; Hratchian, H. P.; Izmaylov, A. F.; Bloino, J.; Zheng, G.; Sonnenberg, J. L.; Hada, M.; Ehara, M.; Toyota, K.; Fukuda, R.; Hasegawa, J.; Ishida, M.; Nakajima, T.; Honda, Y.; Kitao, O.; Nakai, H.; Vreven, T.; Jr; Peralta, J. E.; Ogliaro, F.; Bearpark, M.; Heyd, J. J.; Brothers, E.; Kudin, K. N.; Staroverov, V. N.; Kobayashi, R.; Normand, J.; Raghavachari, K.; Rendell, A.; Burant, J. C.; Iyengar, S. S.; Tomasi, J.; Cossi, M.; Rega, N.; Millam, J. M.; Klene, M.; Knox, J. E.; Cross, J. B.; Bakken, V.; Adamo, C.; Jaramillo, J.; Gomperts, R.; Stratmann, R. E.; Yazyev, O.; Austin, A. J.; Cammi, R.; Pomelli, C.; Ochterski, J. W.; Martin, R. L.; Morokuma, K.; Zakrzewski, V. G.; Voth, G. A.; Salvador, P.; Dannenberg, J. J.; Dapprich, S.;

- Daniels, A. D.; Farkas; Foresman, J. B.; Ortiz, J. V; Cioslowski, J.; Fox, D. J. *Gaussian 09 Revision A.02*; Gaussian Inc. Wallingford CT 2009, 2009.
- (34) Becke, A. *J. Chem. Phys.* **1993**, *98*, 5648–5652.
- (35) Lee, C.; Yang, W.; Parr, R. G. *Phys. Rev. B* **1988**, *37*, 785–789.
- (36) Dolg, M.; Wedig, U.; Stoll, H.; Preuss, H. *J. Chem. Phys.* **1987**, *86*, 866.
- (37) Hratchian, H. P.; Schlegel, H. B. *J. Chem. Theory Comput.* **2005**, *1*, 61–69.
- (38) Hratchian, H. P.; Schlegel, H. B. *J. Chem. Phys.* **2004**, *120*, 9918–9924.
- (39) Yamaguchi, K.; Jensen, F.; Dorigo, A.; Houk, K. N. *Chem. Phys. Lett.* **1988**, *149*, 537–542.
- (40) Wittbrodt, J. M.; Schlegel, H. B. *J. Chem. Phys.* **1996**, *105*, 6574–6577.
- (41) Grimme, S. *J. Comput. Chem.* **2006**, *27*, 1787–1799.
- (42) Marenich, A. V; Cramer, C. J.; Truhlar, D. G. *J. Phys. Chem. B* **2009**, *113*, 6378–6396.
- (43) Ribeiro, R. F.; Marenich, A. V; Cramer, C. J.; Truhlar, D. G. *J. Phys. Chem. B* **2011**, *115*, 14556–14562.
- (44) Scholes, G. D.; Curutchet, C.; Mennucci, B.; Cammi, R.; Tomasi, J. *J. Phys. Chem. B* **2007**, *111*, 6978–6982.
- (45) *Advances in Chemical Physics*; Prigogine, I.; Rice, S. A., Eds.; John Wiley & Sons, Inc.: Hoboken, NJ, USA, 1999; Vol. 106.
- (46) Marcus, R. A. *J. Chem. Phys.* **1956**, *24*, 966.
- (47) Perdew, J. P. *Phys. Rev. B* **1981**, *23*, 5048–5079.
- (48) Zhang, Y.; Yang, W. *J. Chem. Phys.* **1998**, *109*, 2604.
- (49) Lundberg, M.; Siegbahn, P. E. M. *J. Chem. Phys.* **2005**, *122*, 224103.
- (50) Johansson, A. J.; Blomberg, M. R. A.; Siegbahn, P. E. M. *J. Chem. Phys.* **2008**, *129*, 154301.
- (51) Swart, M.; Groenhof, A. R.; Ehlers, A. W.; Lammertsma, K. *J. Phys. Chem. A* **2004**, *108*, 5479–5483.
- (52) Swart, M. *J. Chem. Theory Comput.* **2008**, *4*, 2057–2066.
- (53) Güell, M.; Solà, M.; Swart, M. *Polyhedron* **2010**, *29*, 84–93.

- (54) Radoń, M. *J. Chem. Theory Comput.* **2014**, *10*, 2306–2321.
- (55) Ji, L.; Faponle, A. S.; Quesne, M. G.; Sainna, M. A.; Zhang, J.; Franke, A.; Kumar, D.; van Eldik, R.; Liu, W.; de Visser, S. P. *Chem. Eur. J.* **2015**, *21*, 9083–9092.
- (56) Harvey, J. N.; Aschi, M.; Schwarz, H.; Koch, W. *Theor. Chem. Acc.* **1998**, *99*, 95–99.
- (57) Acuña-Parés, F.; Codolà, Z.; Costas, M.; Luis, J. M.; Lloret-Fillol, J. *Chem. Eur. J.* **2014**, *20*, 5696–5707.
- (58) Acuña-Parés, F.; Costas, M.; Luis, J. M.; Lloret-Fillol, J. *Inorg. Chem.* **2014**, *53*, 5474–5485.
- (59) Codolà, Z.; Garcia-Bosch, I.; Acuña-Parés, F.; Prat, I.; Luis, J. M.; Costas, M.; Lloret-Fillol, J. *Chem. Eur. J.* **2013**, *19*, 8042–8047.
- (60) Prat, I.; Mathieson, J. S.; Güell, M.; Ribas, X.; Luis, J. M.; Cronin, L.; Costas, M. *Nat. Chem.* **2011**, *3*, 788–793.
- (61) Karamzadeh, B.; Singh, D.; Nam, W.; Kumar, D.; de Visser, S. P. *Phys. Chem. Chem. Phys.* **2014**, *16*, 22611–22622.
- (62) De Visser, S. P.; Tan, L. S. *J. Am. Chem. Soc.* **2008**, *130*, 12961–12974.
- (63) Kumar, S.; Faponle, A. S.; Barman, P.; Vardhaman, A. K.; Sastri, C. V.; Kumar, D.; de Visser, S. P. *J. Am. Chem. Soc.* **2014**, *136*, 17102–17115.
- (64) Zavitsas, A. A. *J. Org. Chem.* **2008**, *73*, 9022–9026.
- (65) De Visser, S. P. *J. Am. Chem. Soc.* **2010**, *132*, 1087–1097.
- (66) Kumar, D.; Karamzadeh, B.; Sastry, G. N.; de Visser, S. P. *J. Am. Chem. Soc.* **2010**, *132*, 7656–7667.
- (67) Kumar, D.; Latifi, R.; Kumar, S.; Rybak-Akimova, E. V.; Sainna, M. A.; de Visser, S. P. *Inorg. Chem.* **2013**, *52*, 7968–7979.
- (68) Ye, S.; Geng, C.-Y.; Shaik, S.; Neese, F. *Phys. Chem. Chem. Phys.* **2013**, *15*, 8017–8030.
- (69) Decker, A.; Rohde, J.-U.; Klinker, E. J.; Wong, S. D.; Que, L.; Solomon, E. I. *J. Am. Chem. Soc.* **2007**, *129*, 15983–15996.
- (70) Sahu, S.; Widger, L. R.; Quesne, M. G.; De Visser, S. P.; Matsumura, H.; Moënné-Loccoz, P.; Siegler, M. A.; Goldberg, D. P. *J. Am. Chem. Soc.* **2013**, *135*, 10590–10593.

- (71) Tsuzuki, S. *Annu. Reports Prog. Chem. Sect. C: Phys. Chem.* **2012**, *108*, 69.
- (72) Alamiddine, Z.; Humbel, S. *Front. Chem.* **2013**, *1*, 37.
- (73) Kozuch, S.; Shaik, S. *Acc. Chem. Res.* **2011**, *44*, 101–110.
- (74) Houle, F. A.; Beauchamp, J. L. *J. Am. Chem. Soc.* **1979**, *101*, 4067–4074.
- (75) Janardanan, D.; Usharani, D.; Chen, H.; Shaik, S. *J. Phys. Chem. Lett.* **2011**, *2*, 2610–2617.

For Table of Contents Only:



The reaction mechanisms for alkane oxidation processes catalyzed by non-heme Fe^{VO} complexes presented in literature vary from rebound stepwise to concerted highly asynchronous processes. Herein it is showed that the nature of the substrate and solvent (or gas phase) explains the variety of different mechanisms for the hydroxylation of alkanes catalyzed by non-heme iron complexes reported in the literature.